Available online at www.sciencedirect.com

SCIENCE DIRECT®

Journal of Computational Physics 198 (2004) 35–64

JOURNAL OF COMPUTATIONAL PHYSICS

www.elsevier.com/locate/jcp

An interface interaction method for compressible multifluids

X.Y. Hu [a,*], B.C. Khoo [a,b]

[a] Singapore-MIT Alliance, 4 Engineering Drive 3, 117576 Singapore, Singapore
[b] Department of Mechanical Engineering, National University of Singapore, 119260 Singapore, Singapore

Received 15 January 2003; received in revised form 4 December 2003; accepted 19 December 2003

Abstract

In the development of numerical schemes for compressible multifluids, the treatment of the interface is very important. In this paper, we proposed a numerical method based on interface interactions where the ghost cells of the ghost fluid method, GFM [J. Comput. Phys. 152 (1999) 457], are determined by solving the real interface interaction and the hypothetical "ghost" interaction. Extensive tests in 1D are carried out and with the 2D examples suggest that the present scheme is able to handle multifluids problems with large difference of states and material properties at interface while still keeping to the simplicity of the original GFM.

---

1. Introduction

Various numerical methods have been developed to simulate and study the dynamics of compressible multifluids in a wide range of high speed flow phenomena, such as the dynamics and the stability of shock interface interaction, supersonic mixing processes, high speed bubbly flows, underwater explosion and many others. Invariably, a relative dominant difficulty for these numerical computations is the treatment of material interfaces. For Eulerian schemes, in general, there are two main approaches: one is the rather complicated *front tracking method* in which the interface is tracked as an internal moving boundary and a non-smeared interface can be materialized [15,16]; the other is the relatively simpler *front capturing method* in which the interface is defined as a steep gradient and hence the latter is allowed to be smeared over a narrow band. For the latter, some specific examples are VOF (volume-of-fluid) (see [1,21,41]) and CIP (constrained-interpolation-profile) (see [40]). Even though the interest in the present work concerns compressible multifluids, it may be mentioned that these methods have been also used for incompressible fluids. Still, there are other methods for interface treatment, such as the immersed boundary method [23] and phase field method [14], which are usually employed for incompressible multifluids.

---

[*] Corresponding author. Tel.: +65-68744797; fax: +65-67752920.
E-mail addresses: xiangyu_hu@yahoo.com.cn, smahx@nus.edu.sg (X.Y. Hu), mpekbc@nus.edu.sg (B.C. Khoo).

doi:10.1016/j.jcp.2003.12.018

To obtain a non-smeared interface and avoid the complexity of front tracking, the employment of level set function enables a combination of the above-mentioned two approaches [30], in which the interface is treated as inner boundaries and the front movement is captured by a level set function. In the original work by Mudler et al. [28], the interface is still allowed to be smeared to a certain thickness artificially. In [7,6,25,26], smearing at the interface is avoided by solving the Riemann problem to correct for the numerical flux near the interface. However, as noted by Fedkiw et al. [10], these schemes can be and is usually fairly intricate and can perhaps only be extended to multidimension with dimensional splitting in time.

The ghost fluid method (GFM) [10], on the other hand, offers a fairly simple way to implement in multidimension and with multilevel time integrals. This method relies entirely on the abilities to produce ghost cells and their states on the respective medium that satisfy the appropriate boundary conditions at the interface and is proposed to solve the multifluids problem by using standard one-phase solvers for each medium. Therein also lies in the versatility of the GFM in the accommodation of any reasonable and consistent one-phase solvers. While the GFM presents promising results, it may yet face some difficulties when a strong shock wave passes and interacts with the interface [27]. Abgrall and Karni [1] proposed another similar but simpler single fluid method (SFM). However, the SFM may not be so suitable when there is density limitation in the equation of states like Tait's equation for the water medium and it is unclear if this method can handle those difficulties encountered by the GFM. Fedkiw et al. [11] proposed a method which incorporates solving the Rankine–Hugoniot relation pertaining to the detonation or deflagration discontinuity. In a subsequent review, Fedkiw [12] also suggested solving the Riemann problem at the interface. In a separate development, to overcome the difficulties encountered for air–water interaction, Fedkiw [13] presented a modified GFM which also eliminates the oscillations at the air–water interface. However, this modified GFM seems to be air–water interaction specific such that there is a very large sound impedance change across the interface. Recently, Liu et al. [27] proposed a method by solving the shock–shock relation of the Riemann problem near the interface, in which the proposed interface states are applied to locations some distance away from the interface. As the interaction is not solved at the interface, this method may give rise to difficulties in maintaining accuracy at the interface and is also relatively much less straightforward in its implementation and extension to multi-dimensional problems with complex interfaces.

The motivation of this paper stems from the difficulties and concerns of the presence of a sufficiently strong shock in multifluids problem with possible large differences of states and material properties at the interface. We propose a interface interaction method which solves for two types of interaction: one is the real interaction at the interface, the other is a (hypothetical) ghost interaction between the real fluid and ghost fluid. Using the method of characteristics and the interaction solved for directly at the interface, the ghost cell properties for the respective medium are defined within a narrow band next to the interface; the ghost fluid and the real fluid co-exist and the scheme allows for calculation in the interface region as if in a single medium domain just like the original GFM. Therefore, by keeping to the simplicity of the GFM, it is rather straightforward in extending to multi-dimensional problems with complex interfaces. In addition, as suggested in Fedkiw [12], we also propose improved updating of velocity in the level set function calculation for a general interface so as to increase the accuracy of the interface location.

2. Preliminaries

2.1. Euler equations

Assuming the fluid is inviscid and compressible, the flow can be described by Euler equations in two dimensions

$$\begin{pmatrix} \rho \\ \rho u \\ \rho v \\ E \end{pmatrix}_t + \begin{pmatrix} \rho u \\ \rho u^2 + p \\ \rho uv \\ (E+p)u \end{pmatrix}_x + \begin{pmatrix} \rho v \\ \rho uv \\ \rho v^2 + p \\ (E+p)v \end{pmatrix}_y = 0, \tag{1}$$

This set of equations describes the conservation of density ρ, momentum $\rho\mathbf{v} \equiv (\rho u, \rho v)$ and total energy density $E = \rho e + \frac{1}{2}\rho u^2$, where e is the internal energy per unit mass. The one-dimensional Euler equations are obtained by setting $v = 0$.

To close this set of equations, the equation of states (EOS) must be defined to give the relation between pressure, density and internal energy. There are several forms of EOS for different materials, but all can be written generally as $p = p(\rho, e)$. If the entropy is kept constant, an isentropic EOS results and can be written as $p = p(\rho, s_0)$. Here, the pressure is determined by density directly.

2.2. Level set equation

Consider a moving interface $\Gamma(t)$ separating the domain $\Omega(t)$. We associate $\Omega(t)$ with a signed distance function $\phi(x, y, t)$, that is $\nabla|\phi| = 1$, called the level set function [30]. Knowing ϕ we may locate the interface by finding the zero level set of ϕ. That is $\Gamma(t) = \{x, y : \phi(x, y, t) = 0\}$. So the movement of the interface is equivalent to the updating of ϕ. We can use the level set equation

$$\phi_t + u\phi_x + v\phi_y = 0 \tag{2}$$

to update all the level sets, where u and v are the velocity components for the level sets in x and y directions.

For compressible multi-material flows, the interface velocity is usually not known, hence the movement of the zero level set at interface is approximated by updating level sets on the nearest grid points. As the speed near the interface may change very rapidly or become a discontinuity as the interface moves, the solution of Eq. (2) often becomes very flat and/or steep at the interface. Therefore, ϕ needs to be re-initialized to be kept as the signed distance. The re-initialization equation can be written as

$$\phi_\tau + \mathrm{sgn}(\phi)(|\nabla\phi| - 1) = 0, \tag{3}$$

where τ is fictitious time, $\mathrm{sgn}(\phi)$ is a sign function and is usually approximated by a smooth function [31,37]. The equation is updated in fictitious time-step, such as $\Delta\tau = \Delta x/2$. For a given ϕ, this equation can be solved to steady state after sufficient τ-steps. As re-initialization is needed for the whole domain, the fast marching method [34] can also be used to increase efficiency, in which case the Eikonal equation $|\nabla\phi| = 1$ is solved directly. For the flows with strong shock waves, ϕ may need to be re-initialized at every time-step. However, re-initialization at every time-step can lead to the movement of the zero level set and must be performed extremely carefully; otherwise serious difficulties will result, such as large mass loss.

In the computation of compressible multifluids, smooth or constant extension of a quantity q is sometimes needed. For example, in the GFM, flow variables are needed to be extended into the ghost cells. We use the extending equation

$$q_\tau \pm \mathbf{N} \cdot \nabla q = 0 \tag{4}$$

to extend quantities to their neighborhood. Here $\pm\mathbf{N}$ is the positive and negative normal direction of the level set and used to decide the extending direction [10]. $+\mathbf{N}$ is used to extend quantities from regions $\phi < 0$ to regions $\phi > 0$, while $-\mathbf{N}$ is used to extend quantities from regions $\phi > 0$ to regions $\phi < 0$. Again, for a given q, the extending equation can be solved to steady solution.

2.3. Ghost cells

As the interface serves to separate two distinct media, the two associated flow fields are to be solved separately. In a finite difference implementation, special care is needed when the grid points of the difference stencil is cut by the interface. As such, the states on the other side of the interface can not be used directly which can and usually leads to serious oscillations. These "missing" points can be filled by the so called ghost cells (collocated with the real cells but separated by the interface). Therefore, both the two fluids have their own real cells and ghost cells. The presence of ghost cells allows the two fluids to be calculated separately as a single fluid and makes the interface "invisible" during the computation.

The ghost cell can be considered to be first introduced to the front tracking method by Glimm et al. [15], in which the states of the ghost cells are extrapolated from nearby point from the same side. For the GFM based on level set tracking [10], a narrow band of ghost cells is defined in the vicinity of the interface. At the ghost cells, the ghost fluid is defined with the same pressure and normal velocity of the real fluid and the ghost cell density is obtained from constant entropy extrapolation. For the SFM, the ghost cells are defined by directly copying the pressure, normal velocity and density from the real cells. In the modified GFM [13] for the air–water interaction, the normal interface velocity is obtained from the water side and the pressure at the interface is obtained from the air side.

3. The interface interaction method

In our method, the ghost cell states are defined according to the interface interactions. We firstly determine the interface condition. That is, the interface velocity, pressure and densities are obtained by solving the real interface interaction of the two fluids. Then two hypothetical interactions called *ghost interactions* are defined between each ghost fluid and its corresponding real fluid. In each ghost interaction, the real fluid reaches the same interface condition as that of the real interaction. As higher order extrapolation may be used to calculate more accurate states near the interface, the interface condition can also be obtained with higher order accuracy by involving more nodes. Hence, the ghost cell states are also correspondingly evaluated. Therefore, the present method can lead or be extended to a possible higher order for multifluids problems. However, for simplicity, the discussion in this paper is based on the first order extrapolation only.

For this method, we propose two assumptions: (a) the interactions take place at the interface, (b) there is no entropy exchange between the two fluids throughout the interaction. With the first assumption, unlike Liu et al. [27] in which the interaction takes place at some distance away from the interface, the interaction process is controlled by the two fluid states directly at the interface and any other flux into the interaction region is neglected. The second assumption followed that by Fedkiw et al. [10], where there is no heat transfer and mass diffusion through the interface and energy exchange at the interface is only via work. This assumption is applicable even when there is a shock passing through the interface. This is because the interface interaction can be described by a Riemann problem essentially without any entropy exchange. Usually, there are many ways to solve the Riemann problem for the interface interaction, such as the exact Riemann solver and different types of approximate Riemann solvers. In this work, we use the method of characteristics [33] to solve both the real and ghost interactions at the interface.

3.1. Interface condition

Assume that the adjacent grid cells have two different fluids and their states are $W_j = W_\mathrm{l} = (\rho_\mathrm{l}, u_\mathrm{l}, p_\mathrm{l})$ and $W_{j+1} = W_\mathrm{r} = (\rho_\mathrm{r}, u_\mathrm{r}, p_\mathrm{r})$, as shown in Fig. 1. According to the first assumption, as first-order extrapolation is used, the states of the two half-fluid cells nearest to the interface are utilized in the interaction, and the

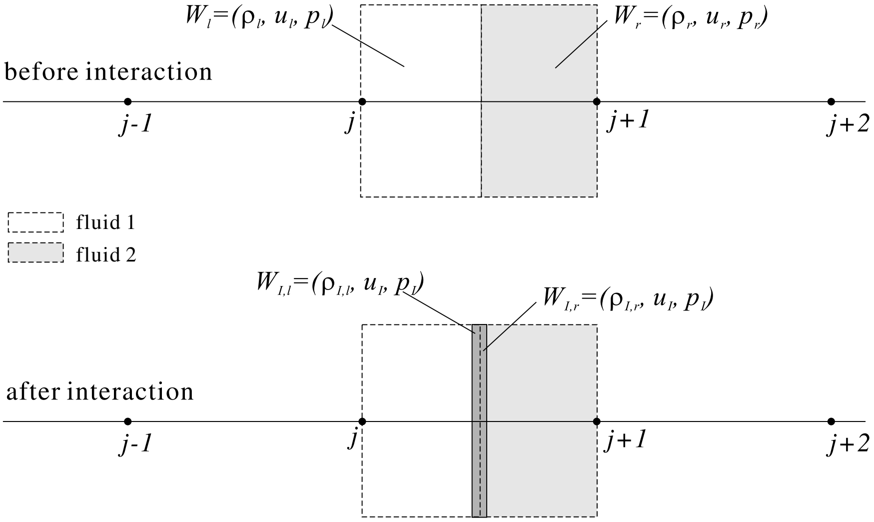

Fig. 1. Schematic for the interface interaction.

interface position remains unchanged (see Fig. 1). In line with the second assumption, different EOSs can be used for the two particular fluids under investigation. After the interaction, the interface takes on the interface velocity u_{I} and pressure p_{I}. The densities of the two fluids near the interface have also changed to $\rho_{\mathrm{I,l}}$ and $\rho_{\mathrm{I,r}}$, respectively. With the method of characteristics, we have the relations

$$u_{\mathrm{I}} = u_{\mathrm{l}} - \int_{p_{\mathrm{l}}}^{p_{\mathrm{I}}} \frac{\mathrm{d}p}{\rho_{\mathrm{I,s}} c_{\mathrm{I,s}}}, \tag{5}$$

$$u_{\mathrm{I}} = u_{\mathrm{r}} + \int_{p_{\mathrm{r}}}^{p_{\mathrm{I}}} \frac{\mathrm{d}p}{\rho_{\mathrm{r,s}} c_{\mathrm{r,s}}}, \tag{6}$$

$$p_{\mathrm{I}} = p_{\mathrm{l}}(\rho_{\mathrm{I,l}}, s_{\mathrm{l}}), \tag{7}$$

$$p_{\mathrm{I}} = p_{\mathrm{r}}(\rho_{\mathrm{I,r}} s_{\mathrm{r}}), \tag{8}$$

where $\rho_{\mathrm{I,s}}$, $c_{\mathrm{I,s}}$ and $\rho_{\mathrm{r,s}}$, $c_{\mathrm{r,s}}$ are the densities and sound speeds determined by the respective isentropic EOS, $p = p_{\mathrm{l}}(\rho, s_{\mathrm{l}})$ and $p = p_{\mathrm{r}}(\rho, s_{\mathrm{r}})$. Here s_{l} and s_{r} are the respective constant entropies on the left and right sides of the interface. The unknown variables u_{I}, p_{I}, $\rho_{\mathrm{I,l}}$ and $\rho_{\mathrm{I,r}}$ can be obtained by solving Eqs. (5)–(8). In Appendix A.1, the detailed method for the gas–gas and gas–water interface conditions are described.

3.2. Defining the ghost cells

Suppose the real cell state $W_{\mathrm{l}} = (\rho_{\mathrm{l}}, u_{\mathrm{l}}, p_{\mathrm{l}})$ in the left cell j interacts with the ghost cell state $W_{\mathrm{gl}} = (\rho_{\mathrm{gl}}, u_{\mathrm{gl}}, p_{\mathrm{gl}})$ in the right cell $j+1$, as shown in Fig. 2. Both the real and ghost cells are treated with the same EOS as for the left medium. The same assumptions are also applicable to the ghost interaction at the cell wall $j + 1/2$ which takes on the functional role as the interface. After the ghost interaction, the interface assumes the velocity u_{g} and pressure p_{g}. The densities of the two sides at the cell wall are also changed to $\rho_{\mathrm{g,l}}$ and $\rho_{\mathrm{g,gl}}$, respectively. We set the interface velocity, pressure and density on the real fluid side to be equal to

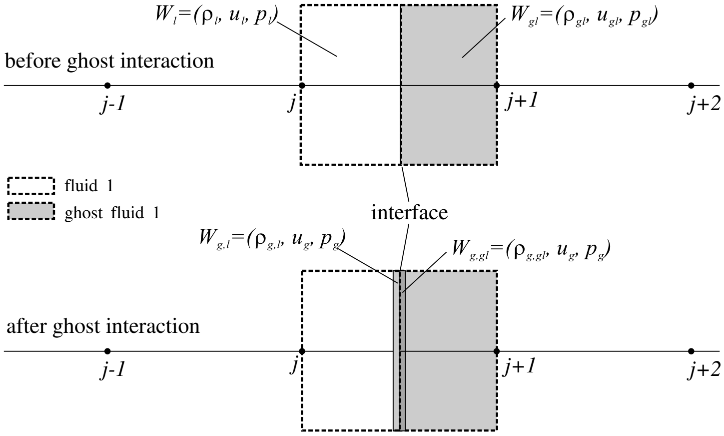

Fig. 2. Schematic for defining the ghost cells.

those after the real interaction, i.e. $u_g = u_I$, $p_g = p_I$, and $\rho_{g,l} = \rho_{I,l}$; this implies that both the ghost and real interactions give the *same* interface condition for the real fluid. Therefore, the ghost cell states can be obtained by solving

$$u_I = u_{gl} + \int_{p_{gl}}^{p_I} \frac{dp}{\rho_{gl,s} c_{gl,s}}, \tag{9}$$

$$p_{gl} = f_s(\rho_{gl}, s_{gl}), \tag{10}$$

with the given interface condition of u_I and p_I. Here $\rho_{gl,s}$ and $c_{gl,s}$ are the density and sound speed determined by the isentropic EOS on the left medium, and s_{gl} is the ghost cell entropy throughout the interaction. However, one may note that there is no unique solution for the ghost interaction problem. While Eqs. (9) and (10) are satisfied, the ghost cell states may be different by choosing various combinations of two variables from density, pressure or velocity. Here, we shall consider two simplest cases:

- *Algorithm A*

  We define the ghost cell pressure as that at the interface after the real interaction, i.e.

  $$p_{gl} = p_I. \tag{11}$$

  Hence the integral in Eq. (9) becomes zero and the ghost cell velocity is

  $$u_{gl} = u_I. \tag{12}$$

  Furthermore, one can find that any ghost cell density can satisfy Eq. (9). We define the ghost cell density by isentropic extrapolating, i.e. $s_{gl} = s_l$. Therefore, the ghost cell density on the right side can be computed directly by $p_{gl} = f_s(\rho_{gl}, s_l)$. See Appendix A.2 for details on gas–gas and gas–water interactions.
- *Algorithm B*

  We define the ghost cell pressure and density by constant extending, i.e.

  $$p_{gl} = p_l, \tag{13}$$

  $$\rho_{gl} = \rho_l. \tag{14}$$

Hence, from Eqs. (5) and (9), we obtain the ghost cell velocity as

$$u_{\mathrm{gl}} = 2u_{\mathrm{I}} - u_{\mathrm{l}}. \tag{15}$$

As the real and ghost fluids have the same pressure after the ghost interaction (see Fig. 2), via isentropic condition, we have

$$\rho_{\mathrm{I,l}} = \rho_{\mathrm{g,gl}} \tag{16}$$

for both Algorithm A and B. One can find further that the above two cases are equivalent for the ghost interactions because both the real and ghost fluid give rise to the *same* interface conditions of velocity, pressure and densities. It may be noted that the ghost cell states in Algorithm B has the same form of the boundary conditions as for a moving piston (see also [20,9]. Therefore, one may interpret that the physical meaning or outcome of the two algorithms as if the interface is treated as a piston and the velocity of the moving piston is determined by the interface interaction. One may also find that, from the interface condition, the energy exchange rate between the two fluids is $p_{\mathrm{I}}u_{\mathrm{I}}$; this is the same as that between the real and ghost fluids for the same p_{I} and u_{I} are obtained from the ghost interaction. In the numerical tests of Section 6, it is found that Algorithm B faces some difficulties when there is strong rarefaction wave near the interface (Case I-A and Case II-A) even though it works well for the other problems considered. In our implementation, we primarily use Algorithm A to determine the ghost cell states for its greater robustness. It may noted that our attention is brought to the very recent work of Arienti et al. [2] who used a piston-like boundary to solve for the fluid-structure interaction problem. However, it differs from Algorithm B in that the interface velocity for the latter is calculated by solving the Riemann problem not applicable to former.

Similarly, for the real cell state $W_{\mathrm{r}} = (\rho_{\mathrm{r}}, u_{\mathrm{r}}, p_{\mathrm{r}})$ in cell $j+1$, the ghost cell state $W_{\mathrm{gr}} = (\rho_{\mathrm{gr}}, u_{\mathrm{gr}}, p_{\mathrm{gr}})$ in cell j can also be defined by a ghost interaction with the EOS on the right. To avoid possible "over heating" errors, an isobaric fix [9,10] is introduced from $j-1$ to j and $j+2$ to $j+1$ before solving the interface interaction problem. For the gas medium, the isentropic fix for one node near the interface seems sufficient for our method. For the water medium, the isobaric fix is not used as Tait's equation is only dependent on pressure. For nodes to the left of j or the right of $j+1$, the ghost states are simply extended or isentropic extrapolated from W_{gl} and W_{gr}, respectively. Choosing either presents no significant difference for the final results.

Here, we make the following observations:

- Besides the simplicity, the other reason we propose Algorithm A among the various non-unique solutions of Eqs. (9) and (10) is because of its generality. In Algorithm A the ghost density can be arbitrarily defined while still keeping to the interface condition. This makes the algorithm easily employed with different types of EOS even those with density limitation.
- Although the above algorithms are proposed based on the method of characteristics, it may be noted that other interface interaction solvers can also be implemented. For example, algorithms can be formulated based on exact or even other approximate Riemann solver in a similar fashion as for the present method of characteristics. The basic idea remains that of real and ghost interactions giving rise to the same interface condition as for the real fluid and hence determining the ghost cell properties. In this paper, the method of characteristics is suggested for its simplicity and ease of implementation. As will be shown in Section 6, the method of characteristics is deemed sufficient to produce reasonable results which concur with analysis even for very stiff problems.
- In the present method, as the ghost cell density is different from the real density, there is strictly no conservation kept at each time-step. However, we expect the conservation error can be reduced or mitigated because the conservation properties is also controlled by a moving piston boundary condition. This will be discussed further in Section 6.4 based on specific numerical examples.

4. Implementation in multidimension

For one dimension, the above interface interaction method is simple and easily implemented. For higher dimensions, as more velocities components are involved, we only need to consider the interface interaction in the normal direction to the interface and hence the normal velocity component is required. In the procedure below, with respect to the direction normal to the interface (or interaction), we shall define the cells with $\phi < 0$ as on the left and the cells with $\phi > 0$ as on the right.

1. Extend p, ρ, u, v along the normal direction to the ghost cells in a narrow band near the interface for the two fluids using Eq. (4).
2. Calculate the normal velocities of the all the cells in the narrow band.
3. Solve the interface conditions for the real interaction along the normal direction via Eq. (5) to Eq. (8).
4. Compute the ghost cell state values by solving the ghost interaction given in Eq. (9) to Eq. (15).
5. Update the ghost cell velocity components by replacing the normal velocity components obtained from the ghost interaction.
6. Update the real cell values of the two fluids separately using the respective one-phase solvers.

5. Modification of level set updating

As the interface velocity has been computed at the interface, the zero level set is then moving at the exact interface velocity. Therefore, we update the zero level set function in Eq. (2) with solved interface velocity. This has also been employed by Fedkiw et al. [11] for the detonation waves and suggested by Fedkiw [12]. As the more accurate advection velocity is used, the re-initialization procedure is not implemented for the immediate region next to the interface. The re-initialization is only needed for the regions away from narrow band to maintain a signed distance to the interface. The level set updating with the main solver is given as follows:

1. Calculate the interface conditions for all cells in the narrow band and set the calculated interface velocity for level set updating.
2. Set the ghost cell values, and update the whole flow fields.
3. Update the level set via Eq. (2) only in the narrow band.
4. Re-initialize the level set via Eq. (3) for cells outside the narrow band.

The TVD Runge–Kutta method [35] may be used for time integration where a full time-step is made up of several sub-time-steps. While the interface condition and the ghost cell values may be computed at every sub-time-step, the the level set updating and re-initialization are computed once in the full time-step. As the calculated interface velocities in the narrow band are very close, the τ-steps for Eq. (3) can be reduced comparing to that of the GFM [10]. Usually, one can only requires about five τ-steps to give a good signed distance function.

6. Numerical examples

The following numerical examples are provided to illustrate the ability of the interface interaction method, which is denoted as I-GFM, to handle multifluids with large difference of states and material properties at the interface. We shall denote the original ghost fluid method as GFM [10], the single fluid method as SFM [1], and the modified ghost fluid method as M-GFM [13]. For all the test cases, unless otherwise stated, the one-phase calculations are carried with fifth-order WENO-LF which is a robust high order conservative scheme [22,36] and third-order TVD Runge–Kutta method [35]. Before the three sub-time-steps of TVD Runge–Kutta method, the interface condition is solved once. After the ghost states are defined, the time-steps for the two fluid regions including ghost cells are calculated separately under Courant–Friedrich–Lewy time-step restriction; the smaller one is chosen as the overall time-step. For the one-dimensional examples, unless otherwise stated, the number of grid points employed is 200 and the referenced exact solution is sampled on 200 grid points too. All the runs are carried out with the CFL of 0.6.

6.1. Shock tube problems (I)

Case I-A: We consider a air–helium shock tube problem with the following initial data:

$$(\rho, u, p, \gamma) = \begin{cases} (1, 0, 1, 1.4) & \text{if } x < 0.5, \\ (0.125, 0, 0.1, 1.667) & \text{if } x > 0.5. \end{cases} \tag{17}$$

The typical results at time $t = 0.15$ computed with the I-GFM with Algorithm A (denoted as I-GFM-A), GFM, SFM and I-GFM with Algorithm B (denoted as I-GFM-B) are shown in Fig. 3. One can observe that the I-GFM-A shows good compatibility with the original GFM and gives almost identical and correct shock strength and speed. The interface position is also captured accurately. One may also note that the SFM exhibits a slight degree of smearing at the contact discontinuity of the density plot. While the I-GFM-B predicts a broadly correct solution, it introduces larger errors at the location of the rarefaction wave. Further numerical tests show that the stronger the rarefaction wave near the interface, the larger is the discrepancy from analysis. For interactions with very strong rarefaction wave, such as for Case II-A in Section 6.3, Algorithm B faces much difficulties. The results of other problems without the presence of strong rarefaction waves depict almost similar behavior as for Algorithm A, such as for Cases I-B, I-C and I-D (not shown here). For the subsequent results presented, all the computations are carried out with Algorithm A for greater robustness. It may be note that the computations with the M-GFM give rise to large discrepancies with analysis whether the pressure or velocity is copied from the left or the right sides (not shown here). This is perhaps not unexpected since the M-GFM is originally designed specifically for air–water interface where there is a very large sound impedance change across the interface and may not be so directly applicable to the present gas–gas interaction problem in the absence of such said large sound impedance change. For this reason, for the following examples of gas–gas interaction, only the results of I-GFM, GFM and SFM are discussed.

Case I-B: We compute for a more stiff shock tube problem which is taken from Abgrall and Karni [1]. The initial data are

$$(\rho, u, p, \gamma) = \begin{cases} (1, 0, 500, 1.4) & \text{if } x < 0.5, \\ (1, 0, 0.2, 1.667) & \text{if } x > 0.5. \end{cases} \tag{18}$$

The results at time $t = 0.015$ using the I-GFM, GFM and SFM are shown in Fig. 4. One can find the the results of the I-GFM are in good agreement with the exact solution. For the GFM, there are some discrepancies found near the interface. More numerical viscosity is also produced for the SFM, which leads to greater smearing at the shock front; it requires a much finer distribution of about 800 grid points to ensure sharper shock front comparable to that of the I-GFM or GFM [1]. For both the GFM and SFM, one can also observe the overshoots at the end of the rarefaction waves on the velocity profiles. Abgrall and Karni suggested that these are due to the difficulties associated with the one-phase solver and not the multifluid modeling. It may be mentioned that, with the I-GFM, the overshoot is replaced by a very mild undershoot even though all the three methods use the same WENO scheme for the one-phase solver (see the velocity plot in Fig. 4).

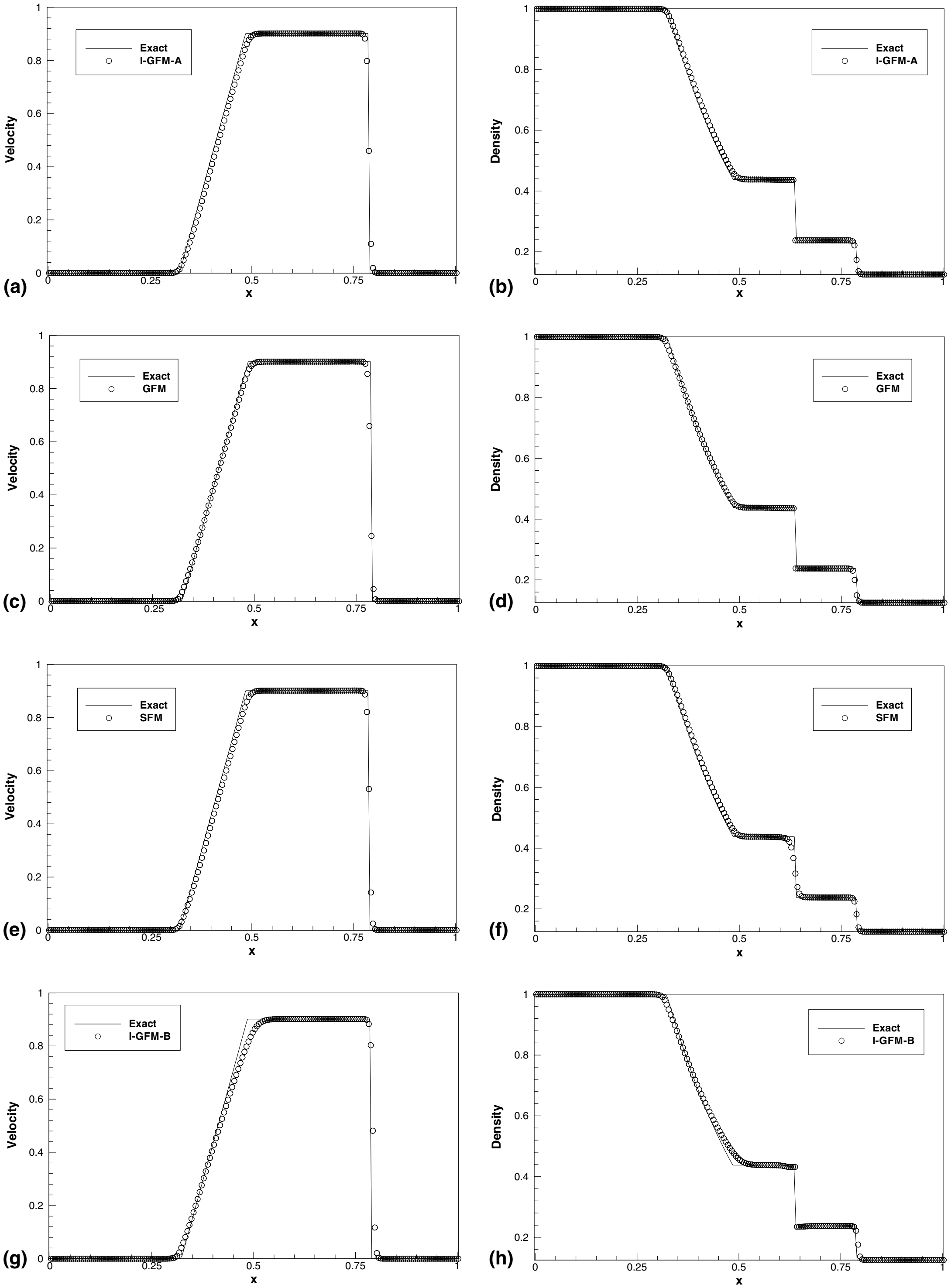

Fig. 3. Shock tube problem: Case I-A.

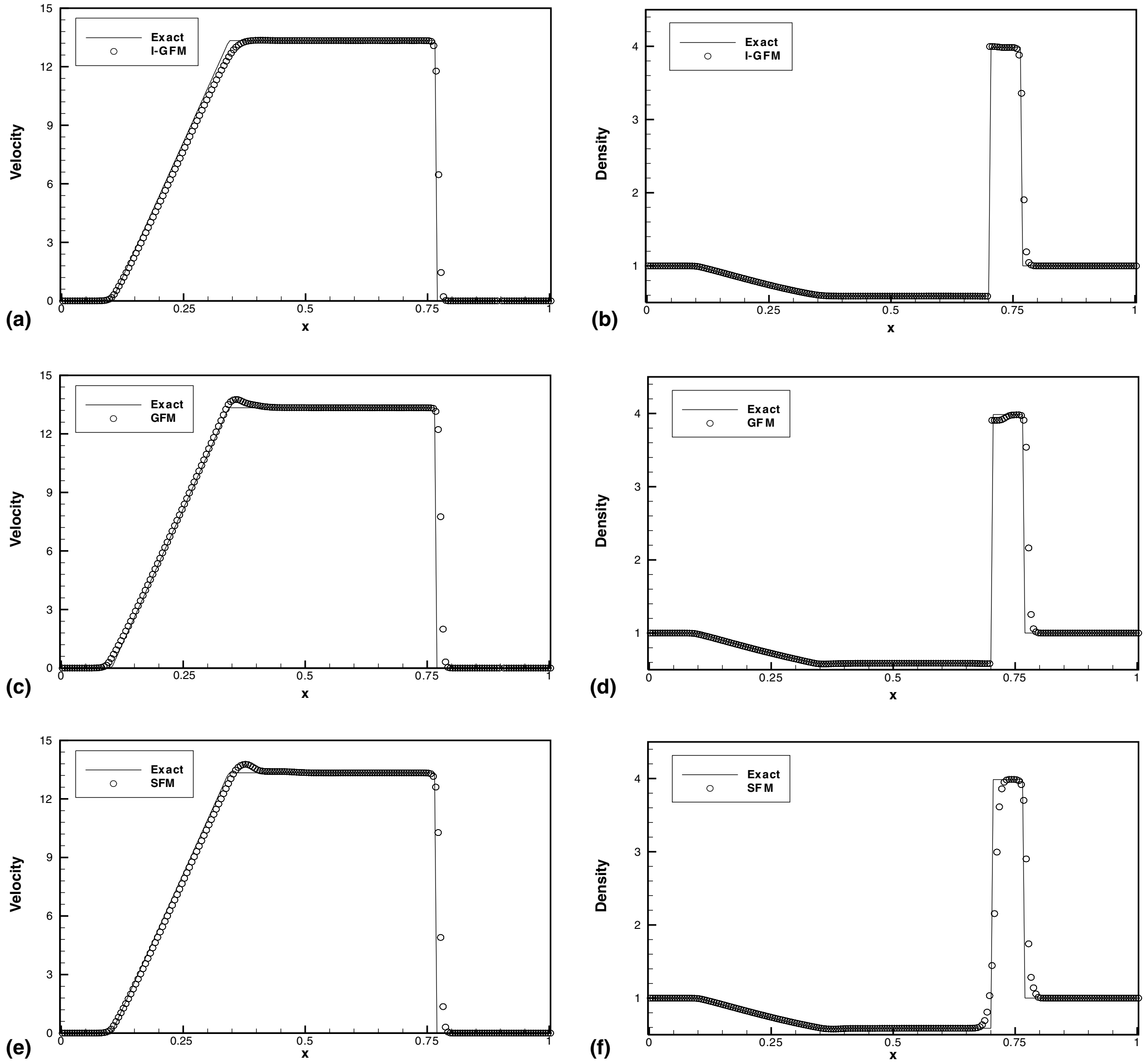

Fig. 4. Shock tube problem: Case I-B.

Case I-C: For this case, we greatly increase the ratio of initial density by up to an order of magnitude, that is

$$(\rho, u, p, \gamma) = \begin{cases} (1, 0, 500, 1.4) & \text{if } x < 0.8 \\ (10, 0, 0.2, 1.667) & \text{if } x > 0.8. \end{cases} \tag{19}$$

There is a greater stiffness in the problem due to the larger difference of densities near the interface. We run this case to a final time of 0.02. The results using the I-GFM, GFM and SFM are shown in Fig 5. One can find that the results of the I-GFM are in reasonably good agreement with the exact solution. For the GFM , there are some discrepancies for the rarefaction wave which shows a non-physical wave moving from the right to the left. For the SFM, one can find the large numerical viscosity cause much smearing to the shock front. In addition, the discrepancy at the end of the rarefaction wave increases to an almost unacceptable level which produces a large hump in the velocity profile.

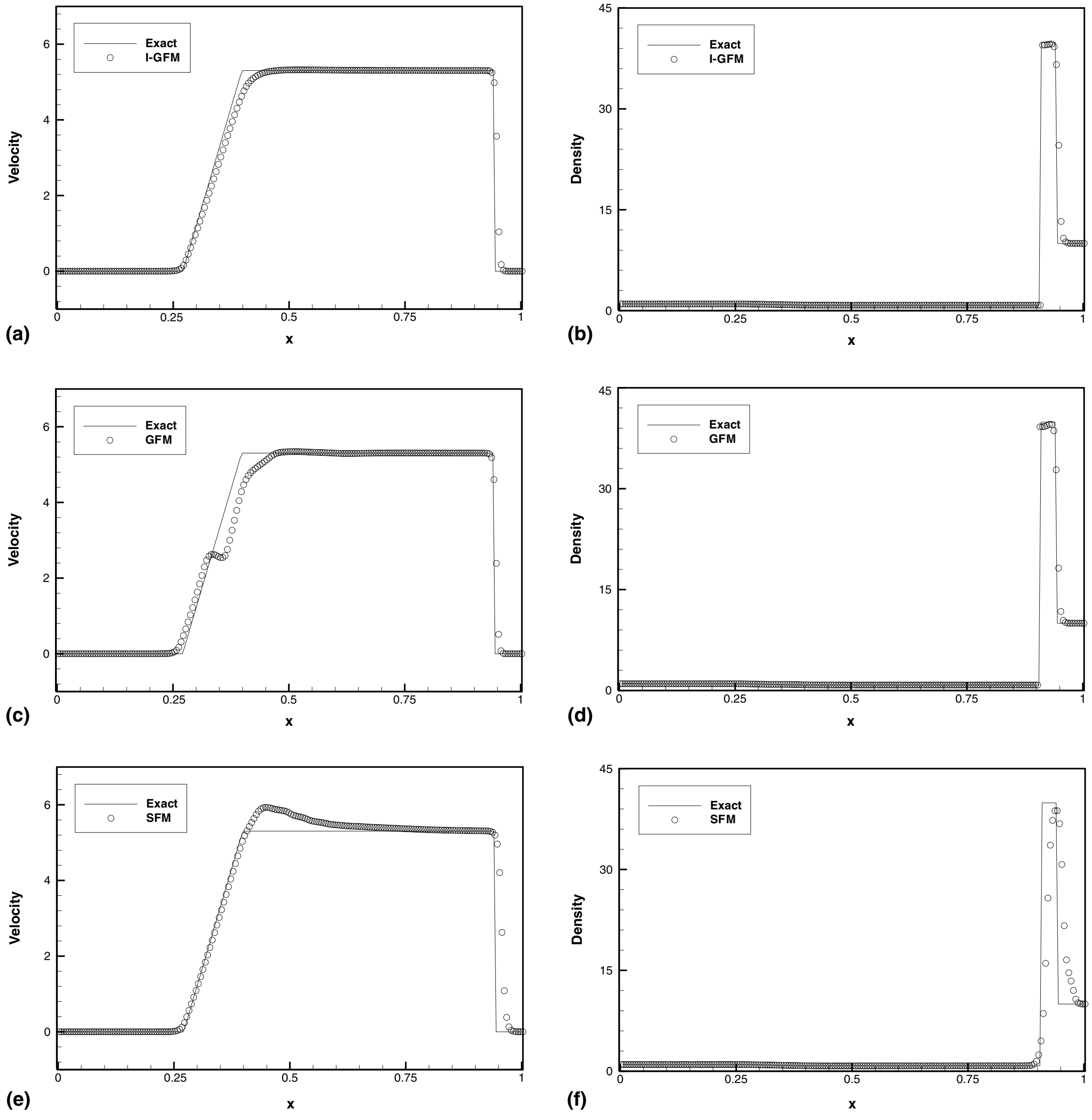

Fig. 5. Shock tube problem: Case I-C.

Case I-D: In this case, we change the magnitude of density and γ on the right side, such that

$$(\rho, u, p, \gamma) = \begin{cases} (1, 0, 500, 1.4) & \text{if } x < 0.75 \\ (30, 0, 0.2, 2.0) & \text{if } x > 0.75. \end{cases} \tag{20}$$

As both the initial difference of density and heat ratio at the interface becomes ever larger, this problem is very stiff. Fig. 6 shows the typical results by the I-GFM and GFM at time $t = 0.02$. One can find that the results with the I-GFM depict still reasonable agreement with the exact solution. For the results obtained

$$(\rho, u, p, \gamma) = \begin{cases} (3.984, 27.355, 1000, 1.667) & \text{if } x < 0.2, \\ (0.01, 0, 1, 1.4) & \text{if } x > 0.2. \end{cases} \tag{21}$$

The typical results shown using the I-GFM, GFM and SFM are plotted in Fig. 7 for $t = 0.01$. For the I-GFM, the comparison with exact solution shows good agreement. For both the GFM and SFM, there are some discrepancies of the calculated interface position and shock wave speed when compared to the exact solution. It is also apparent that the GFM depicts some undershoot or overshoot towards the reflected rarefaction wave end (see the velocity and density plots in Fig. 7).

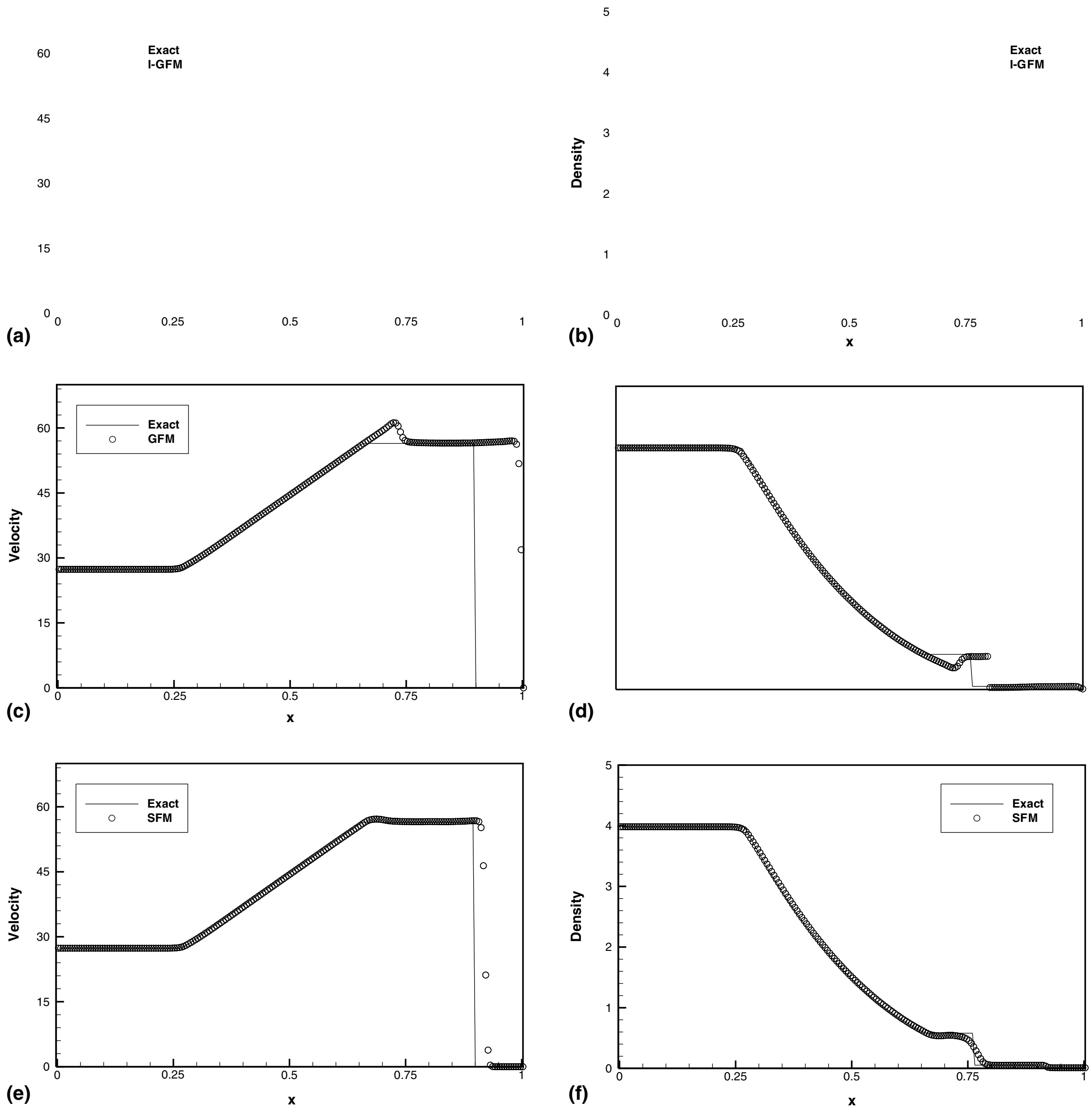

Fig. 7. Shock interface interaction problem: Case II-A.

Case II-B: We consider a strong shock wave with a pressure ratio of 100 propagating from a helium-like gas to an air-like gas. The initial conditions are very similar to that taken from Liu et al. [27] except that the density ratio is more severe with much larger quantity pertaining to the air-like gas. The initial data are

$$(\rho, u, p, \gamma) = \begin{cases} (0.384, 27.077, 100, 1.667) & \text{if } x < 0.6, \\ (10, 0, 1, 1.4) & \text{if } x > 0.6. \end{cases} \tag{22}$$

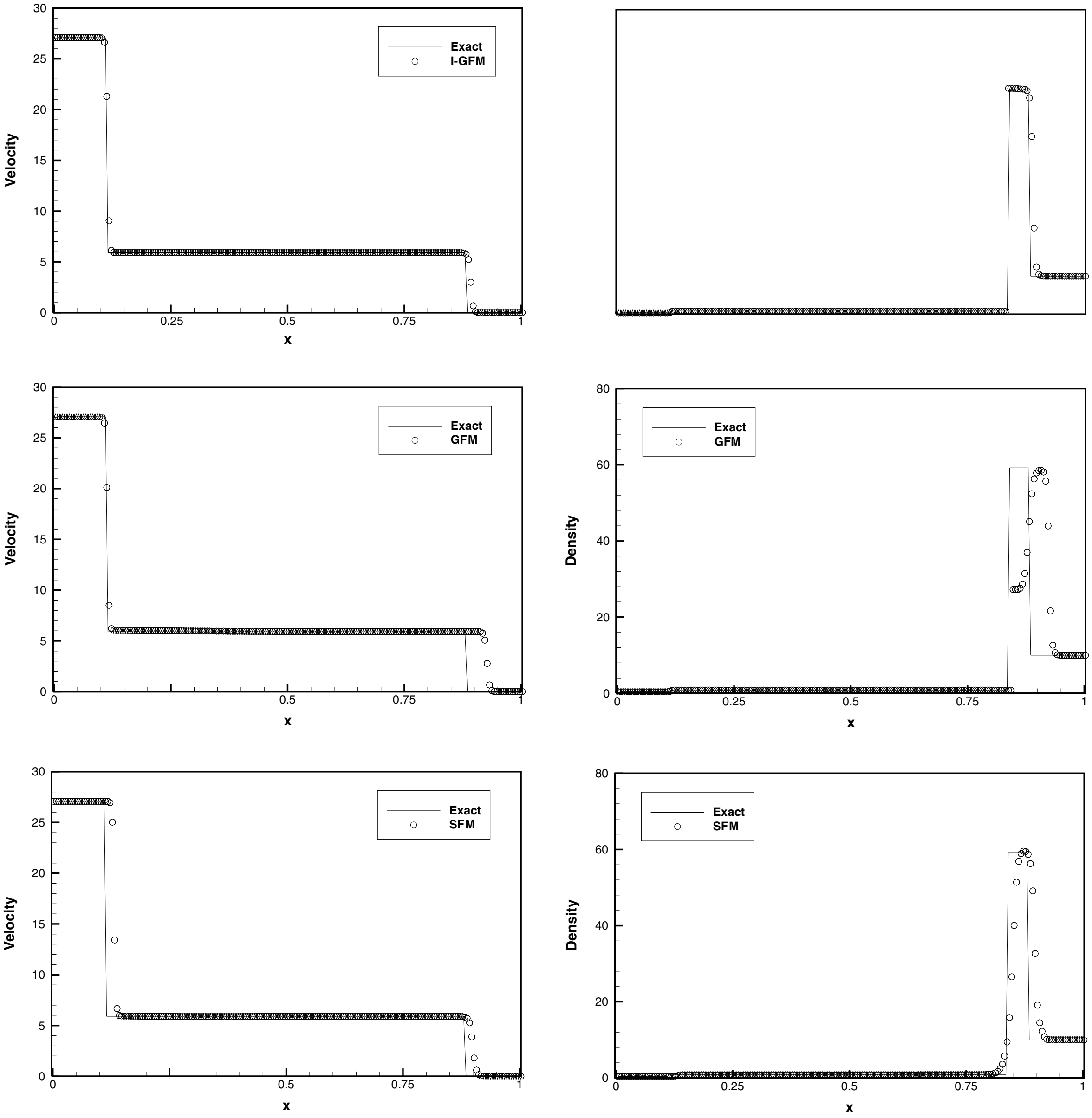

The results obtained at time $t = 0.04$ using the I-GFM, GFM and SFM are shown in Fig. 8. The results of the I-GFM compare well with the exact solution. Both the GFM and SFM predict the transmitted shock and interface speed which have larger variance with the analysis.

Case II-C: The initial density ratio at the interface is increased by another order of magnitude together with an increase of the heat ratio. The initial condition is given as

$$(\rho, u, p, \gamma) = \begin{cases} (0.384, 27.077, 100, 1.667) & \text{if } x < 0.6. \\ (100, 0, 1, 3.0) & \text{if } x > 0.6. \end{cases} \tag{23}$$

Fig. 9 shows the results using the I-GFM and SFM at time $t = 0.03$. The results with I-GFM still compare very well with the exact solution. On the other hand, the computation via the GFM faces difficulties. For the SFM, it can still compute for this problem but with much smeared interface and transmitted shock wave front (see Fig. 9(c) and (d)). It is noted that the Algorithm B can calculate for Case II-B and Case II-C without difficulty and gives almost identical results as for Algorithm A since there is only shock–shock interaction involved at the interface.

Case II-D: We consider the two blast wave interaction problem which is taken from Woodward and Colella [39]. This is an one-phase problem and the two interfaces are located near the ends of the domain. The initial data are

$$(\rho, u, p, \gamma) = \begin{cases} (1, 0, 1000, 1.4) & \text{if } x < 0.1, \\ (1, 0, 0.01, 1.4) & \text{if } 0.1 < x < 0.9, \\ (1, 0, 100, 1.4) & \text{if } x > 0.9, \end{cases} \tag{24}$$

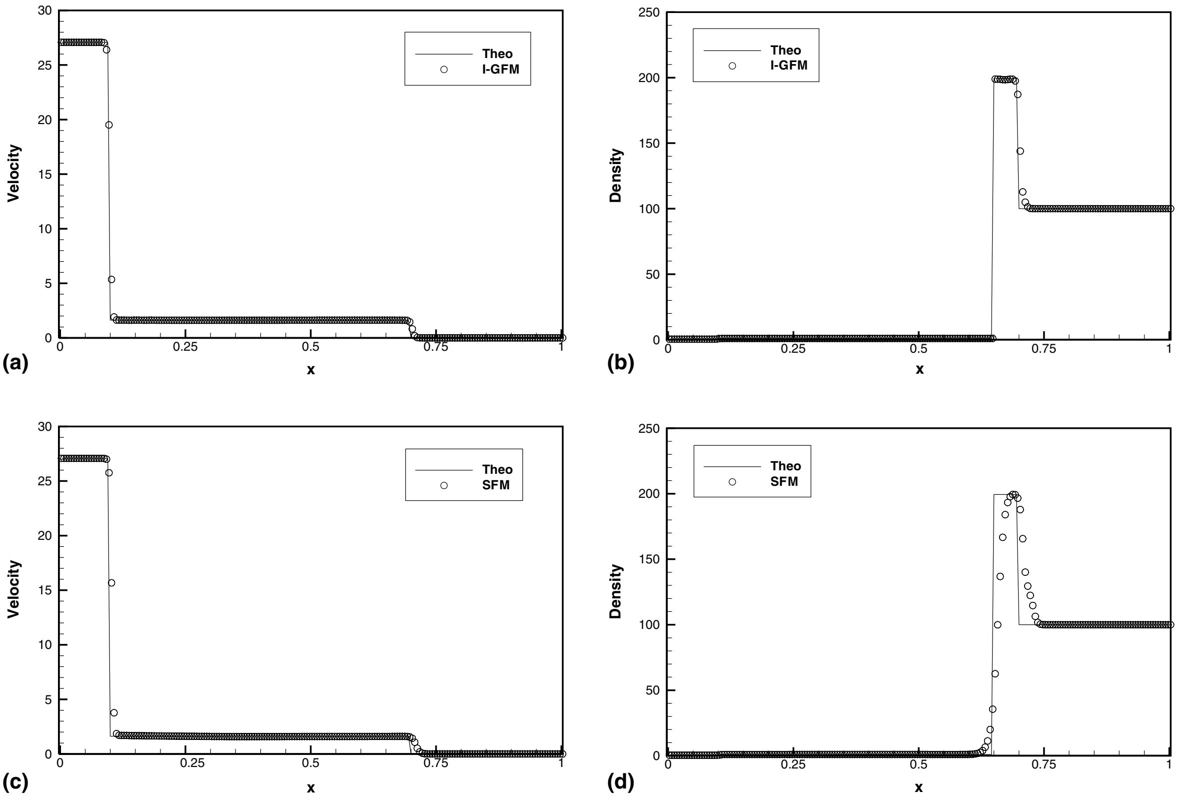

Fig. 9. Shock interface interaction problem: Case II-C.

and reflect
on a 400
points. Fig
similar res
interfaces
which wou
and Shu [

[redacted]

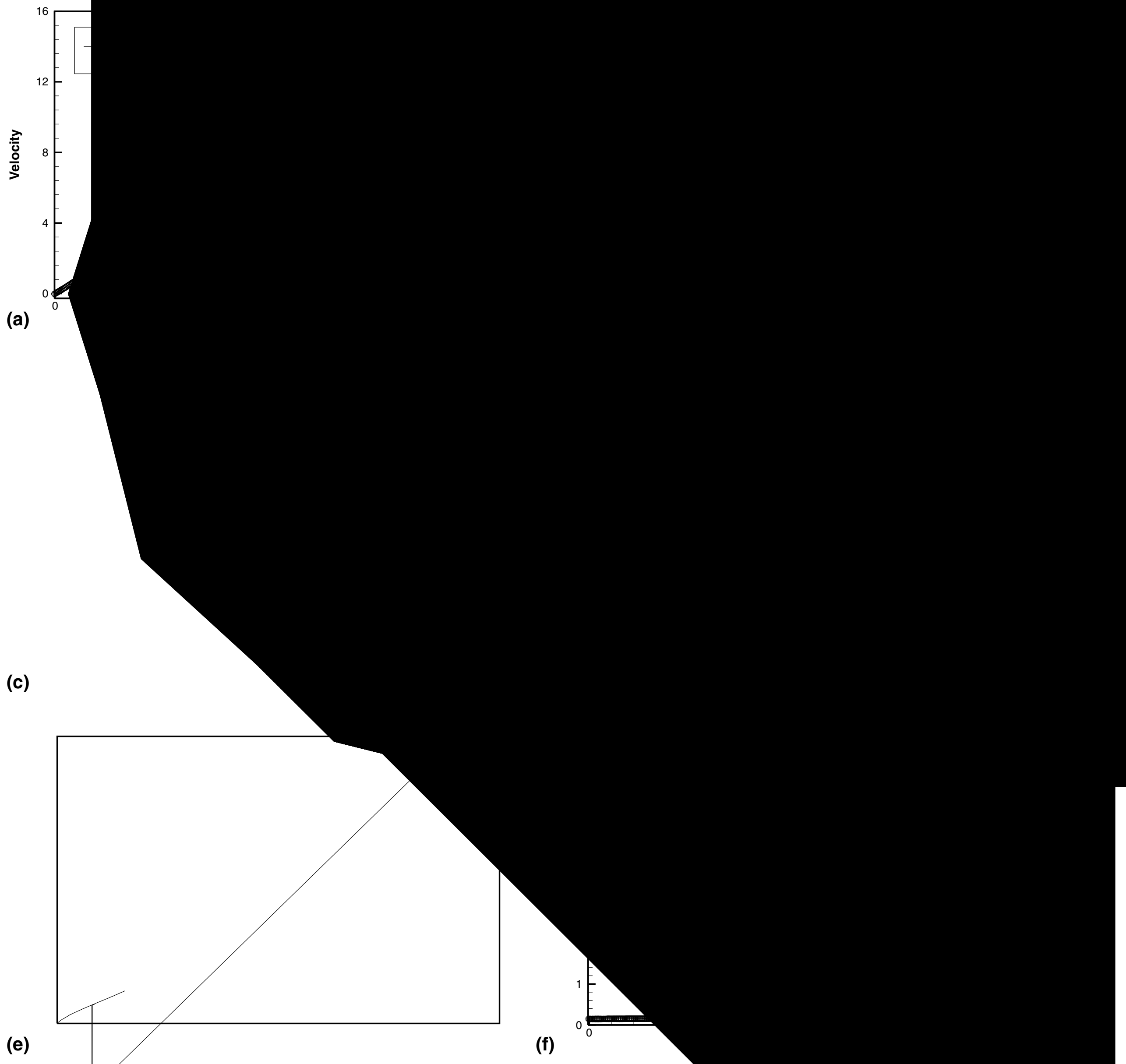

Fig. 10. Shock interface interaction problem: Case I

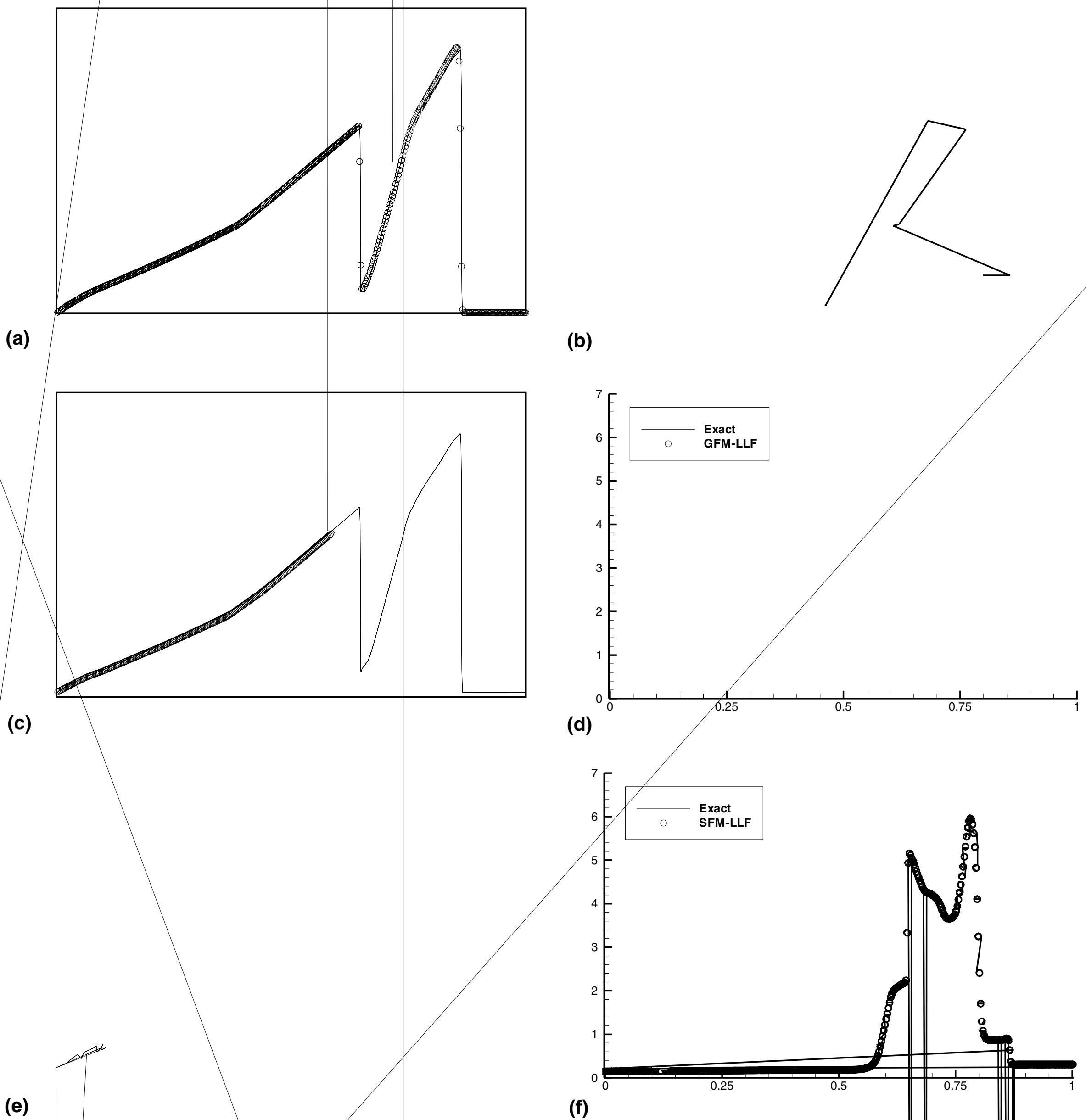

Fig. 11. Solution of Case II-D with WENO-LLF scheme.

For the GFM, there appears to be a non-physical "glitch" in the velocity profile near the right shock front since the shock interactions should not have propagated to this region as yet. However, by carefully tracking and analyzing the evolution process, it is found the "glitch" originates from a strong velocity overshoot produced in the solution of the right shock tube problem and reflected from the right boundary; this is found to be largely mitigated for the I-GFM. If the one-phase solver is changed to WENO-LLF, as the strong velocity overshoot does not occur, the "glitch" disappears almost completely (see Fig. 11). If the

I-GFM is implemented with WENO-LLF, there is further improvement (see also Fig. 11). It is noted that the slight overshoot at the right shock wave is eliminated. As the SFM directly use the real states as for the ghost cell states, when the method is used to solve one-phase problem with contact discontinuity, it behaves like an the original one-phase solver and gives the results with smeared density jumps. While a similar strong velocity overshoot occurs and is reflected from the left boundary, there is a "glitch" at about $x = 0.7$. However, this "glitch" is diminished but still not totally eliminated when WENO-LLF is used (see Figs. 10 and 11).

By this example case, one may suggest that, even though the WENO-LF is supposed to ensure robustness by defining a numerical flux based on global maximum wave speed, it seems to produce more discrepancies in the multifluids computations than the WENO-LLF. While the GFM may sometimes produces improved results by using WENO-LLF, our numerical experiments suggest a much less dependency on the choice of WENO-LF or WENO-LLF for the SFM and I-GFM. Furthermore, the I-GFM seems to be able to capture the correct solution more accurately irrespective of the two schemes.

6.3. Shock interaction with water (III)

In this section, two problems of shock interaction with water are computed. In both cases, Tait's EOS is used for the water medium. The state values are non-dimensionalized with respect to the property of water at 1 atmosphere and length scale 1 m. Only M-GFM which is specially formulated for the air–water problems and the I-GFM are used to calculate these cases.

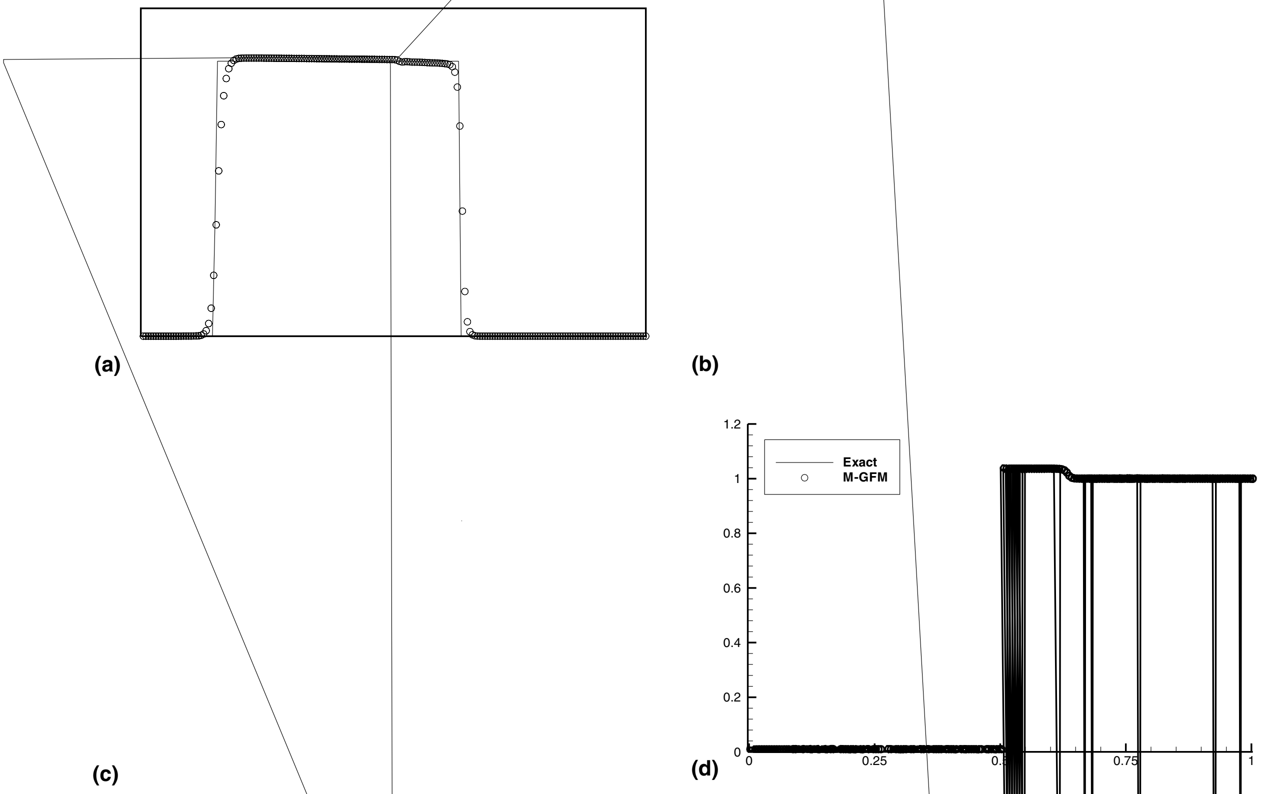

Fig. 12. Problem on shock interaction with water: Case III-A.

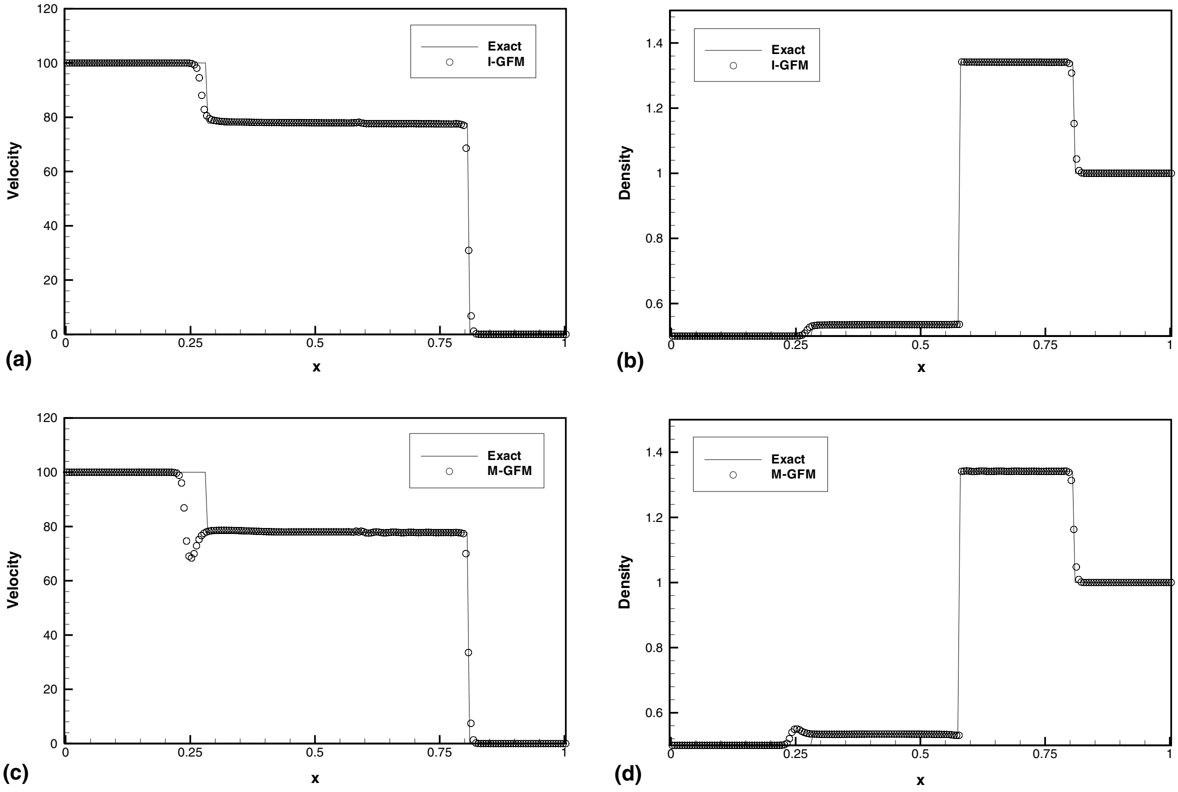

Fig. 13. Problem on shock interaction with water: Case III-B.

Case III-A: This underwater explosion problem is taken from Tang and Huang [38]. The initial condition is given as

$$(\rho, u, p, \gamma) = \begin{cases} (0.01, 0, 1000, 2) & \text{if } x < 0.5, \\ (1, 0, 1, 7.15) & \text{if } x > 0.5. \end{cases} \tag{25}$$

Fig. 12 shows the computed results using I-GFM and M-GFM at time $t = 0.0008$. One can find that both methods give essentially the correct shock wave strength and speed in water. The I-GFM, however, seems to present a slightly more accurate solution for the rarefaction wave.

Case III-B: We increase the energy of the explosives such that the initial pressure ratio is increased by at least one order of magnitude. The initial conditions are

$$(\rho, u, p, \gamma) = \begin{cases} (0.5, 100, 20000, 2.5) & \text{if } x < 0.5, \\ (1, 0, 1, 7.15) & \text{if } x > 0.5. \end{cases} \tag{26}$$

The obtained results by the I-GFM and M-GFM at time $t = 0.001$ are shown in Fig. 13. Note that the strength and speed of the two shock waves are reasonably predicted with the I-GFM. For the M-GFM, one can find that the reflected shock wave in the explosive products has a non-physical front. These results suggest that the M-GFM may produce large errors when implemented directly to the gas–water interaction with less sound impedance difference than that between air and water. In Appendix A.1, one can further find that the M-GFM is a special case of the linearized form of I-GFM.

6.4. Conservation and convergence test

In this section, we perform the conservation and convergence tests for the I-GFM. Based on the particular Case I-A, we compute and compare the conservation errors incurred by the I-GFM, GFM and SFM. Then the convergence property of the I-GFM on mesh refinement is calculated and discussed for the other typical Case I-A to Case I-D.

For the above-mentioned Case I-A to Case I-D, the relative mass and energy variations for the separated left medium and right medium during the computation can be simply calculated by

$$V = \frac{\left(\sum_{j=0}^{j=K^n} U_j^n + f^n U_{\mathrm{I}}^n\right)\Delta x}{\left(\sum_{j=0}^{j=K^0} U_j^0 + f^0 U_{\mathrm{I}}^0\right)\Delta x}, \tag{27}$$

where U_j is the mass density or energy density on cell j, U_{I} is the corresponding quantity at the interface, the superscript 0 and n are for the initial condition and the nth time-step values, respectively, K is the number of cells fully occupied by the left or right medium and f is its volume fraction at the interface, which is based

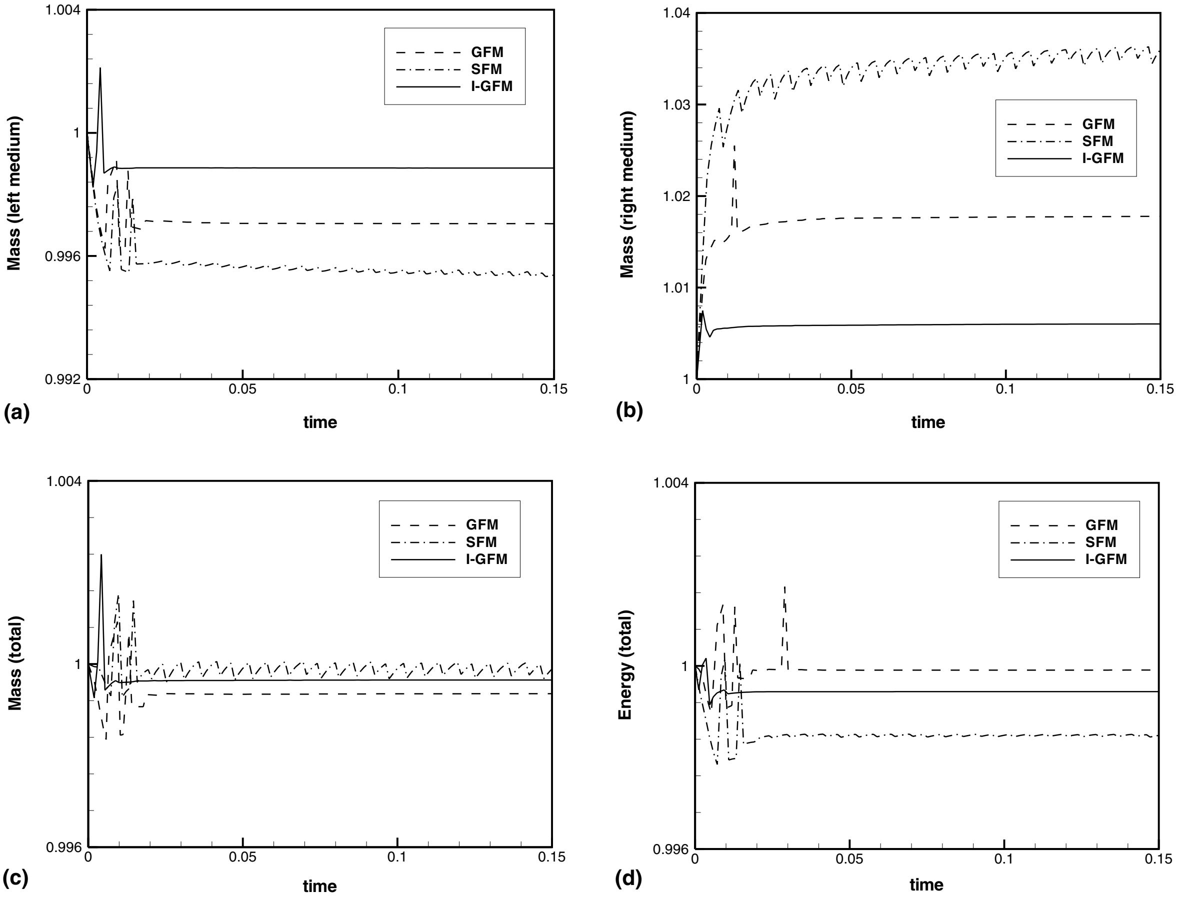

Fig. 14. Relative conservation variation of mass and energy for Case I-A.

on the the zero level set position by linear interpolation. In a similar way, the total mass and energy variations are given as

$$V_{\mathrm{total}} = \frac{\left[(\sum_{j=0}^{j=K^n} U_j^n + f^n U_{\mathrm{I}}^n)_{\mathrm{left}} + (\sum_{j=0}^{j=K^n} U_j^n + f^n U_{\mathrm{I}}^n)_{\mathrm{right}} \right] \Delta x}{(\sum_{j=0}^{j=K^0} U}$$

this additional step undertaken, it has led to an improvement of results [29]. For the I-GFM, as it still predicts a reasonably accurate solution with smaller conservation errors, it seems that a similar post-processing procedure can be effectively incorporated and be developed to be a fully conservative interface interaction method as well.

6.5. Collapse of 2D air cavity collapse in water

To demonstrate the implementation of the interface interaction method in 2D and verify the assembled code, we perform a numerical simulation of an experiment carried out previously by Bourne and Field [5]: a

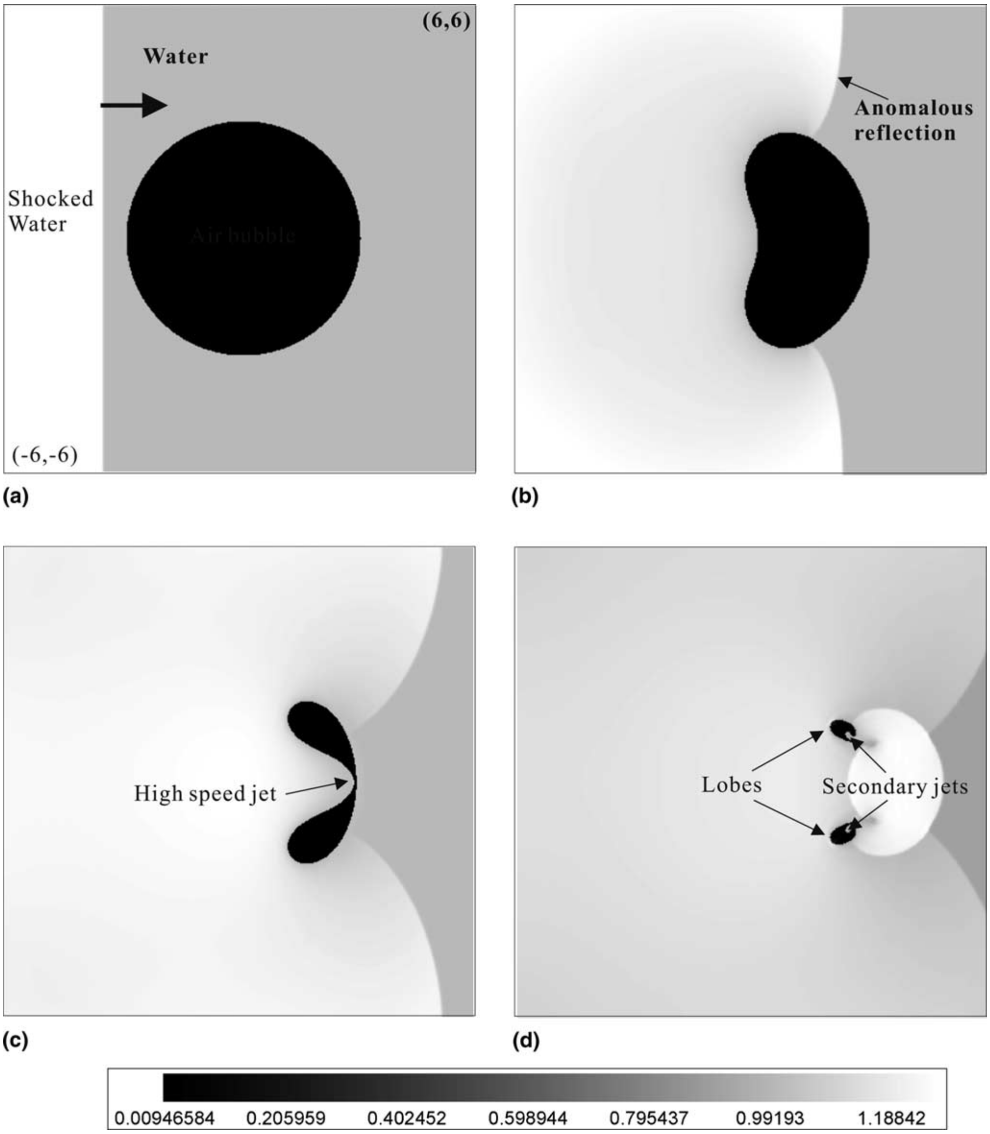

Fig. 15. Collapse of air cavity in water: (a) computational domain and initial conditions, (b) density contours at $t = 2.0 \times 10^{-2}$ (2.0 μs), (c) density contours at $t = 3.1 \times 10^{-2}$ (3.1 μs), and (d) density contours at $t = 3.7 \times 10^{-2}$ (3.7 μs).

6 mm cylinder air cavity in gelatine/water is impacted by a 1.9 GPa shock. The experimental results show that a very high speed jet is formed which then hit the downstream cavity wall. A very high pressure and temperature are also produced at the impact point of the high speed jet. Bourne and Field also observed luminescence in the interaction process. There have been a number of simulations on cylinder cavity collapse under shock [4,8,18]. According to Bourne and Field's experiments, the schematic of the problem is given in Fig. 15(a). All the boundaries are outflow boundaries with zero gradient. The non-dimensionlized (based on the property of water at 1 atmosphere and length scale 1 mm) initial data are

$$\begin{cases} (\rho = 1, u = 0, v = 0, p = 1, \gamma = 7.15) & \text{pre-shocked water,} \\ (\rho = 1.31, u = 67.32, v = 0, p = 19000, \gamma = 7.15) & \text{post-shocked water,} \\ (\rho = 1.2 \times 10^{-3}, u = 0, v = 0, p = 1, \gamma = 1.4) & \text{air bubble,} \\ \phi = -3 + \sqrt{x^2 + y^2} & \text{level set.} \end{cases} \tag{29}$$

Here $\phi \leqslant 0$ represents the air and $\phi > 0$ represents the water. Fig. 15(a) shows an air cavity of radius 3 at $(0, 0)$ is to be impacted by a shock wave initiated at $x = 2.4$. A 400×400 nodes grid is uniformly distributed in the respective x and y directions and the same fifth-order WENO-LF is also used as the one-phase solver. Fig. 15(b)–(d) shows the typical density contours at $t = 0.02$ (2.0 μs), $t = 0.031$ (3.1 μs) and $t = 0.037$ (3.7 μs) after the shock wave impinges on the air cavity. The results are in good agreement with Bourne and Field's [5] observation (their Fig. 5). In Fig. 15(b), the reflected incident wave shows an anomalous reflection pattern. One can also see such similar features as obtained by Grove and Manikoff [18] though for different initial condition. As the cavity collapses the high speed jet is also formed. Fig. 15(c) shows the instance just before the jet making impact on the downstream cavity wall. This result is also in

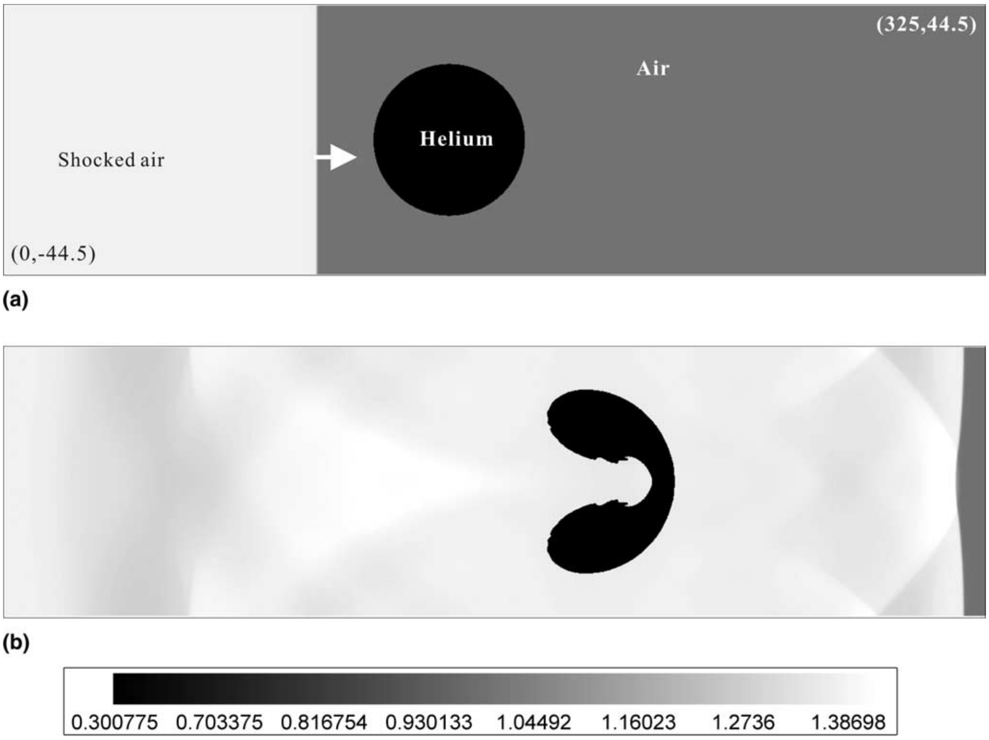

Fig. 16. Air–helium interaction problem: (a) computational domain and initial conditions, (b) density contours at $t = 1.238$ (427 μs).

reasonable agreement with the calculations of Ball et al. [4] using a completely different numerical scheme called the free Lagrange method. However, the present calculated highest jet velocity just before the impact is about 2800 m/s which is some 200 m/s larger than that reported by Ball et al. As the jet impacts on the down stream cavity wall, Ball et al. mentioned that a part of the cavity mass is trapped between the jet nose and cavity wall. However, this is not specifically observed or discussed in the experiments and our numerical results indicate likewise. Our results further show that, after the jet impact, while the resultant strong shock wave interacts with the generated lobes, two secondary jets are also produced (see Fig. 15(d)); the jets subsequently bisect the lobes again to form four separated cavities (not shown here). Finally, when these cavities reaches its smallest volume at about time $t = 4.3$ μs, the calculated temperature in the collapsed cavities is higher than 10,000 K which may be the reason for the presence of luminescence observed in the experiments.

6.6. Air–helium shock interaction

In this 2D problem, we compute for a Mach 1.22 air shock wave interaction with a cylindrical helium bubble. Hass and Sturtevant's [19] experimental results showed that, under the air shock pressure, the helium bubble collapses and a jet is produced. Numerical computations for the same problem can be found in Quirk and Karni [32], Lian and Xu [24] and Bagabir and Drikakis [3]. This problem has also been computed by the original GFM [10]. Fig. 16(a) shows the schematic of the problem, where the upper and the lower boundaries are reflection boundaries of a solid wall. The left and the right boundary condition are outflow boundaries with zero gradient. The non-dimensionlized (based on the property of air at 1 atm and length scale of 1 mm) initial conditions are

$$\begin{cases} (\rho = 1, u = 0, v = 0, p = 1, \gamma = 1.4) & \text{pre-shocked air,} \\ (\rho = 1.3764, u = 0.394, v = 0, p = 1.5698, \gamma = 1.4) & \text{post-shocked air,} \\ (\rho = 0.138, u = 0, v = 0, p = 1, \gamma = 1.667) & \text{helium bubble,} \\ \phi = -25 + \sqrt{(x-150)^2 + y^2} & \text{level set,} \end{cases} \tag{30}$$

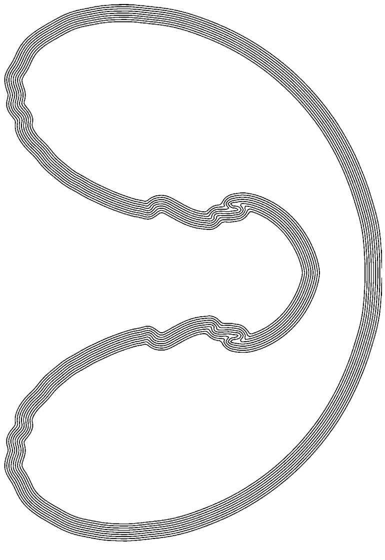

Fig. 17. Level sets near the interface.

where $\phi \leqslant 0$ represents the helium and $\phi > 0$ represents the air, depicting a helium bubble of radius 25 at (0,150) which is to be impacted by a shock wave initiated at $x = 100$. The computation has been carried out with four increasing resolutions of $\Delta x = \Delta y = 2, 1, 0.5, 0.25$; this is also to ensure grid invariance as similarly done in Fedkiw et al. [10]. Similarly, no isobaric fix is used in the calculation to facilitate a quantitative comparison below. It may be added that a separate calculation with isobaric fix has produced essentially similar results with all the characteristics (not shown here); this can be possibly attributed to the not-too-strong incident shock of Mach 1.22.

Fig. 16(b) shows the density contour corresponding to $t = 1.238(427\ \mu\text{s})$ after the air shock makes impact on the helium bubble ($\Delta x = \Delta y = 0.25$). The calculated bubble shape and jet shape are in good agreement with Quirk and Karni's AMR computed results (their Fig. 9(h)) and Hass and Sturtevant's [19] experiment (their Fig. 7(h)). Comparing to the results of the original GFM (Fig. 30 in [10]), one can suggest that the I-GFM calculates more finely the interface details including the jet size and the shape of jet head. This is perhaps to be expected since the interface velocity is accurately calculated and is incorporated directly into the level set evolution. Instabilities are also found at the interface, but, just as in the experiments, they are not as strong as the results of Lian and Xu [24] (their Fig. 4.2) obtained with a front capturing method. Fig. 17 gives the several level sets near the interface at the same time as in Fig. 16(b). It is found that while the accuracy of the zero level set location is kept, the initial property of signed distance is preserved by the equal spacing of the neighboring level sets. Finally, Fig. 18 shows the relative variation of the total helium mass during the computation for the four different resolutions. On can find that the mass

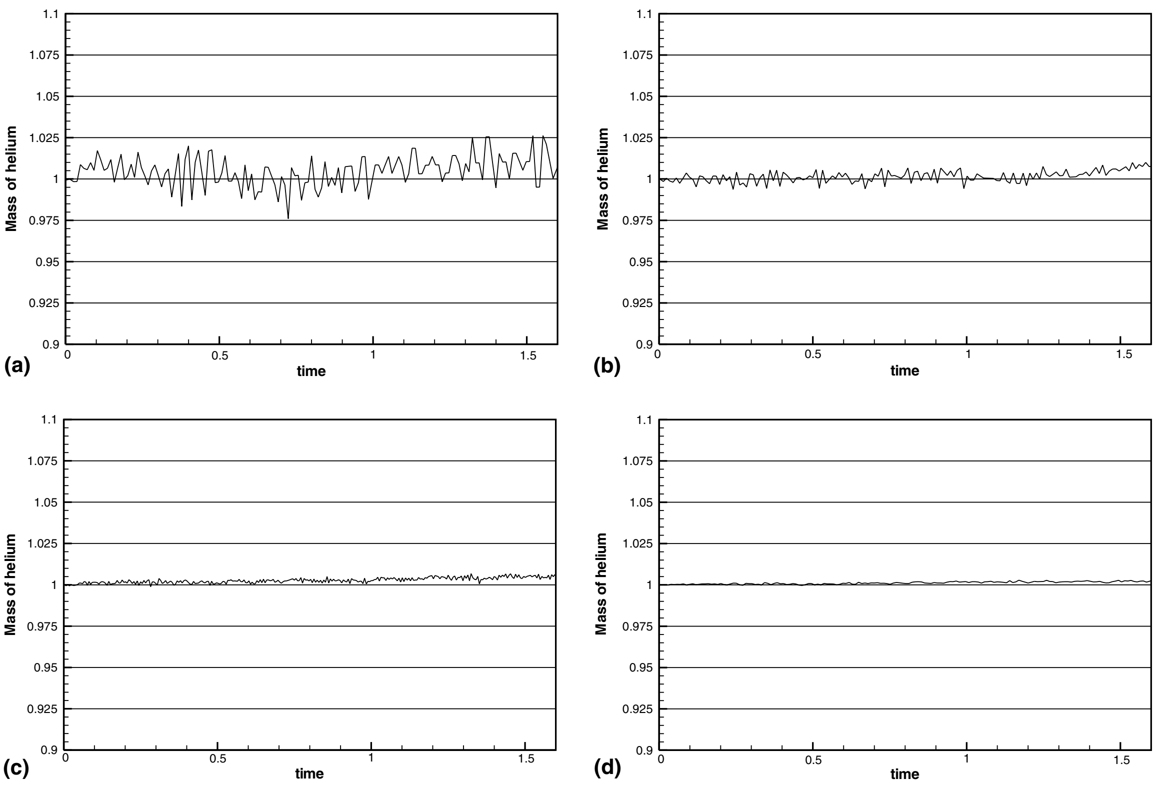

Fig. 18. Normalized helium mass variation from $t = 0$ to about $t = 1.6$ (550 μs): (a) $\Delta x = \Delta y = 2$, (b) $\Delta x = \Delta y = 1$, (c) $\Delta x = \Delta y = 0.5$, and (d) $\Delta x = \Delta y = 0.25$.

conservation error is very small and manageable. This is especially so for the smallest grid size of 0.25. From Fig. 18, the calculated time-averaged relative percentage errors in helium mass (taken w.r.t. the initial quantity at $t = 0$) by our I-GFM are significantly lower than that of the GFM; these values are 0.53%, 0.37%, 0.28% and 0.12% corresponding to the resolutions $\Delta x = \Delta y = 2, 1, 0.5, 0.25$, respectively (which can be compared to 2.5%, 0.78%, 0.42% and 0.43%, respectively, found in [10]). These results further indicates that the I-GFM has good conservation properties.

7. Concluding remarks

In this paper, we developed an interface interaction method based on solving the real and ghost interface interactions. As the method is constructed and modified with respect to the GFM and level set technique, it is simple for implementation and extension to higher dimensions. In the said method, the interface velocity is accurately calculated and the conservation properties are enhanced by the moving piston boundary condition. A number of numerical examples in one dimension are studied with comparisons to exact solution while 2D problems are calculated and compared to experiments and previous methods. The results show that the present method exhibits a greater degree of robustness than the original GFM and SFM. In addition, the interface interaction method is performed only in a narrow band of the mesh and hence is very efficient. The computational cost is almost like the original GFM in most cases. Finally, as the states for solving the interface conditions can be approximated by high order extrapolation, our method may suggest a way for higher accurate schemes for multifluids flows.

Acknowledgements

The authors are indebted to Dr. T.G. Liu and Dr. C.W. Wang, Institute of High Performance Computing, Singapore, for their helps on numerical experiments in the revision of the paper. The authors also wish to thank the three unnamed reviewers for their careful review works and helpful suggestions which led to an improved paper.

Appendix A. Gas–gas and gas–water interaction

A.1. Interface condition

An ideal gas has the EOS of the form

$$p = (\gamma - 1)\rho e, \tag{A.1}$$

where γ is the heat ratio. Tait's EOS for water is

$$p = B\left(\frac{\rho}{\rho_o}\right)^{\gamma} - B + A, \tag{A.2}$$

where $\gamma = 7.15$, $B = 3.31 \times 10^8$ Pa and $A = 1 \times 10^5$ Pa. The isentropic form of ideal gas EOS and the water EOS both can also be written as

$$\frac{f(p)}{\rho^{\gamma}} = \text{Const.}, \tag{A.3}$$

where $f(p) = p$ is for an ideal gas and $f(p) = p + B - A$ is for water. And the equivalent form relating the pressure and sound speed c is

$$S = \frac{2}{\gamma - 1}\ln c + \frac{1}{\gamma}\ln f(p). \tag{A.4}$$

Here S is a constant and $c = \sqrt{\gamma f(p)/\rho}$. To solve the interface condition of Eq. (5) to Eq. (8) can be rewritten as

$$u_{\mathrm{I}} = u_{\mathrm{l}} - \frac{2c_{\mathrm{l}}}{\gamma_{\mathrm{l}} - 1}\left[\left(\frac{f(p_{\mathrm{I}})}{f(p_{\mathrm{l}})}\right)^{(\gamma_{\mathrm{l}}-1)/2\gamma_{\mathrm{l}}} - 1\right], \tag{A.5}$$

$$u_{\mathrm{I}} = u_{\mathrm{r}} + \frac{2c_{\mathrm{r}}}{\gamma_{\mathrm{r}} - 1}\left[\left(\frac{f(p_{\mathrm{I}})}{f(p_{\mathrm{r}})}\right)^{(\gamma_{\mathrm{r}}-1)/2\gamma_{\mathrm{r}}} - 1\right]. \tag{A.6}$$

Eqs. (A.5) and (A.6) can be solved by Newton's method easily.

For flows with limited change of density and sound speed across the interface, the integrals in Eqs. (5) and (6) can be linearized to

$$u_{\mathrm{I}} = u_{\mathrm{l}} - \frac{p_{\mathrm{I}} - p_{\mathrm{l}}}{\rho_{\mathrm{l}} c_{\mathrm{l}}}, \tag{A.7}$$

$$u_{\mathrm{I}} = u_{\mathrm{r}} + \frac{p_{\mathrm{I}} - p_{\mathrm{r}}}{\rho_{\mathrm{r}} c_{\mathrm{r}}}. \tag{A.8}$$

Then u_{I} and p_{I} can be calculated directly as

$$u_{\mathrm{I}} = \frac{\rho_{\mathrm{l}} c_{\mathrm{l}} u_{\mathrm{l}} + \rho_{\mathrm{r}} c_{\mathrm{r}} u_{\mathrm{r}} + p_{\mathrm{l}} - p_{\mathrm{r}}}{\rho_{\mathrm{l}} c_{\mathrm{l}} + \rho_{\mathrm{r}} c_{\mathrm{r}}}, \tag{A.9}$$

$$p_{\mathrm{I}} = \frac{\rho_{\mathrm{l}} c_{\mathrm{l}} p_{\mathrm{r}} + \rho_{\mathrm{r}} c_{\mathrm{r}} p_{\mathrm{l}} + \rho_{\mathrm{l}} c_{\mathrm{l}} \rho_{\mathrm{r}} c_{\mathrm{r}} (u_{\mathrm{l}} - u_{\mathrm{r}})}{\rho_{\mathrm{l}} c_{\mathrm{l}} + \rho_{\mathrm{r}} c_{\mathrm{r}}}. \tag{A.10}$$

For air–water interaction with limited change of pressure and velocity across the interface, the linearized form Eqs. (A.9) and (A.10) degenerates to the modified GFM for the relation $\rho_{\mathrm{water}} c_{\mathrm{water}} \gg \rho_{\mathrm{air}} c_{\mathrm{air}}$.

A.2. Ghost cell values

The ghost cell pressure and velocity are directly copied from the interface conditions. The ghost density ρ_{gl} is solved by relation Eq. (A.3), that is

$$\rho_{\mathrm{gl}} = \rho_{\mathrm{l}}\left(\frac{f(p_{\mathrm{gl}})}{f(p_{\mathrm{l}})}\right)^{1/\gamma}. \tag{A.11}$$

References

[1] R. Abgrall, S. Karni, Computations of compressible multifluids, J. Comput. Phys. 169 (2001) 594.

[2] M. Arienti, P. Hung, E. Morano, J.E. Shepherd, A level set approach to Eulerian–Lagrangian coupling, J. Comput. Phys. 185 (2003) 213.

[3] A. Bagabir, D. Drikakis, Mach number effects on shock-bubble interaction, Shock Waves 11 (2001) 209.

[4] G.J. Ball, B.P. Howell, T.G. Leighton, M.J. Schofield, Shock induced collapse of a cylinder air cavity in water: a free Lagrange simulation, Shock Waves 10 (2000) 265.

[5] N.K. Bourne, J.E. Field, Shock induced collapse of single cabities in liquids, J. Fluid Mech. 244 (1992) 225.

[6] J.P. Cocchi, R. Saurel, A Riemann problem based method for the resolution of compressible multimaterial flows, J. Comput. Phys. 137 (1997) 265.

[7] S.F. Davis, An interface tracking method for hyperbolic systems of conservation laws, Appl. Numer. Math. 10 (1992) 447.

[8] Z. Ding, S.M. Gracewski, Behaviour of gas cavity impacted by weak and strong shock waves, J. Fluid Mech. 309 (1995) 183.

[9] R. Fedkiw, A. Marquina, B. Merriman, An isobaric fix for the overheating problem in multimaterial compressible flows, J. Comput. Phys. 148 (1999) 545.

[10] R. Fedkiw, T. Aslam, B. Merriman, S. Osher, A non-oscillatory Eulerian approach to interfaces in multimaterial flows (the ghost fluid method), J. Comput. Phys. 152 (1999) 457.

[11] R. Fedkiw, T. Aslam, S. Xu, The ghost fluid method for deflagration and detonation discontinuities, J. Comput. Phys. 154 (1999) 393.

[12] R. Fedkiw, The ghost fluid method for discontinuities and interfaces, in: E.F. Toro (Ed.), Godunov Methods, Kluwer Academic Publishers, New York, 2001.

[13] R. Fedki, Coupling an Eulerian fluid calculation to a Lagrangian solid calculation with the ghost fluid method, J. Comput. Phys. 175 (2002) 200.

[14] W.L. George, J.A. Warren, A parallel 3D dendritic growth simulator using the phase-field method, J. Comput. Phys. 177 (2002) 264.

[15] J. Glimm, D. Marchesin, O. McBryan, A numerical method for two phase flow with an unstable interface, J. Comput. Phys. 39 (1981) 179.

[16] J. Glimm, J.M. Grove, X.L. Li, N. Zhao, Simple front tracking, in: G.Q. Chen, E. DiBebedetto (Eds.), Contemporary Mathematics, vol. 238, AMS, Providence, RI, 1999.

[17] J. Glimm, X.L. Li, Y.J. Li, N. Zhao, Conservative front tracking and level set algorithms, PNAS 98 (2001) 14198.

[18] J. Grove, R. Manikoff, Anomalous reflection of shock wave at a fluid interface, J. Fluid Mech. 219 (1990) 313.

[19] J.F. Hass, B. Sturtevant, Interaction of weak shock waves with cylinderical and spherical gas inhomogeneities, J. Fluid Mech. 318 (1987) 129.

[20] C. Hirsch, in: Numerical Computation of Internal and External Flows, vol. 2, Wiley, New York, 1990.

[21] C.W. Hirt, B.D. Nichols, Volume of fluid (VOF) method for the dynamics of free boundaries, J. Comput. Phys. 39 (1981) 201.

[22] G.S. Jiang, C.W. Shu, Efficient implementation of weighted ENO schemes, J. Comput. Phys. 126 (1996) 202.

[23] M.C. Lai, C.S. Peskin, An immersed boundary method with formal second-order accuracy and reduced numerical viscosity, J. Comput. Phys. 160 (2000) 705.

[24] Y. Lian, K. Xu, A gas-kinetic scheme for multimaterial flows and its application in chemical reaction, NASA/CR 19990-209364, 1999.

[25] T.G. Liu, B.C. Khoo, K.S. Yeo, The simulation of compressible multi-medium flow, part I: a new methodology with application to 1D gas–gas and gas–water cases, Comput. Fluids 30 (2001) 291.

[26] L.T.G. Liu, B.C. Khoo, K.S. Yeo, The simulation of compressible multi-medium flow, part II: application to 2D underwater shock refraction, Comput. Fluids 30 (2001) 315.

[27] T.G. Liu, B.C. Khoo, K.S. Yeo, Ghost fluid method for strong shock impacting on material interface, J. Comput. Phys. 190 (2003) 651.

[28] W. Mudler, S. Osher, J.A. Sethian, Computing interface motion in compressible gas dynamics, J. Comput. Phys. 100 (1992) 209.

[29] D. Nguyen, F. Gibou, R. Fedkiw, A fully conservative ghost fluid method and stiff detonation waves. In: Proc. of the 12th International Detonation Symposium, San Diego, CA, August 11–16, 2002.

[30] S. Osher, J.A. Sethain, Front propagating with curvature dependent speed: algorithm based on Hamilton–Jaccobi formulation, J. Comput. Phys. 79 (1988) 12.

[31] D. Peng, B. Merriman, S. Osher, H. Zhao, M. Kang, A PDE-based fast local level set method, J. Comput. Phys. 155 (1999) 410.

[32] J.J. Quirk, S. Karni, On the dynamics of shock-bubble interaction, J. Fluid Mech. 318 (1996) 129.

[33] G. Rudinger, Wave Diagrams for Nonsteady Flow in Ducts, Dover, New York, 1969.

[34] J.A. Sethain, Fast marching methods, SIAM Rev. 41 (1999) 199.

[35] C.W. Shu, S. Osher, Efficient implementation of essentially non-oscillatory shock-capturing schemes, J. Comput. Phys. 77 (1988) 439.

[36] C.W. Shu, High order ENO and WENO schemes for computational fluid dynamics, in: T.J. Barth, H. Deconinck (Eds.), High-order Methods for Computational Physics, Springer, Berlin, 1999.

[37] M. Sussman, P. Smereka, S. Osher, A level set approach for computing solutions to incompressible two-phase flow, J. Comput. Phys. 114 (1994) 146.

[38] H.S. Tang, D. Huang, A second-order accurate capturing scheme for 1D inviscid flows of gas and water with vacuum zones, J. Comput. Phys. 128 (1996) 301.

[39] P. Woodward, P. Colella, The numerical simulation of two-dimensional fluid flow with strong shocks, J. Comput. Phys. 54 (1984) 115.

[40] T. Yabe, F. Xiao, T. Utsumi, The constrained interpolation profile method for multiphase analysis, J. Comput. Phys. 169 (2001) 556.

[41] D.L. Youngs, Time-dependent multi-material flow with large fluid distortion, in: K.W. Morton, M.J. Baines (Eds.), Numerical Methods for Fluid Dynamics, Academic Press, New York, 1982.